Manipulation of thin metal film morphology on weakly interacting substrates via selective deployment of alloying species

Andreas Jamnig, Nikolaos Pliatsikas, Gregory Abadias, Kostas Sarakinos

Manipulation of thin metal film morphology on weakly interacting substrates via selective deployment of alloying species

Jamnig, Andreas

2022-05

Jamnig , A , Pliatsikas , N , Abadias , G & Sarakinos , K 2022 , ' Manipulation of thin metal film morphology on weakly interacting substrates via selective deployment of alloying species ' , Journal of vacuum science & technology : an official journal of the American Vacuum Society , vol. 40 , no. 3 , 033407 . https://doi.org/10.1116/6.0001700

http://hdl.handle.net/10138/346310
https://doi.org/10.1116/6.0001700

unspecified
acceptedVersion

Manipulation of thin metal film morphology on weakly-interacting substrates via selective deployment of alloying species

Running title: Manipulation of thin metal film morphology on weakly-interacting substrates via selective deployment of alloying species

Running Authors: Andreas Jamnig et al.

Andreas Jamnig [1,2], Nikolaos Pliatsikas [1,3], Gregory Abadias [2], and Kostas Sarakinos [1,4,a)]

[1] Nanoscale Engineering Division, Department of Physics, Chemistry and Biology, Linköping University, Linköping, SE 581 83, Sweden
[2] Institut Pprime, Département Physique et Mécanique des Matériaux, UPR 3346 CNRS, Université de Poitiers, ENSMA, 11 Boulevard Marie et Pierre Curie, TSA 41123, F86073 Poitiers Cedex 9, France
[3] Department of Physics, Aristotle University of Thessaloniki, GR-54124 Thessaloniki, Greece
[4] Department of Physics, University of Helsinki, P.O. Box 43, FI-00014, Helsinki, Finland

[a)] Electronic mail: kostas.sarakinos@helsinki.fi

We demonstrate a versatile concept for manipulating morphology of thin ($\leq$ 25nm) noble metal films on weakly-interacting substrates, using growth of Ag on SiO_2 as a model system. The concept entails deployment of minority metallic (Cu, Au, Al, Ti, Cr, Mo) alloying species at the Ag-layer growth front. Data from *in situ* and real-time monitoring of the deposition process show that all alloying agents—when deployed together with Ag vapor throughout the entire film deposition—favor two-dimensional (2D) growth morphology, as compared to pure Ag film growth. This is manifested by an increase in the substrate area coverage for a given amount of deposited material in discontinuous layers and a decrease of the thickness at which a continuous layer is formed, though at the expense of a larger electrical resistivity. Based on *ex situ* microstructural analyses, we conclude that 2D morphological evolution under the presence alloying species is

predominantly caused by a decrease of the rate of island coalescence completion during the initial film-formation stages. Guided by this realization, alloying species are released with high temporal precision to selectively target growth stages before and after coalescence completion. Pre-coalescence deployment of all alloying agents yields a more pronounced 2D growth morphology, which for the case of Cu, Al, and Au is achieved without compromising the Ag-layer electrical conductivity. A more complex behavior is observed when alloying atoms are deposited during the post-coalescence growth stages: Cu, Au, Al, and Cr favor 2D morphology, while Ti, and Mo yield a more pronounced three-dimensional (3D) morphological evolution. The overall results presented herein show that targeted deployment of alloying agents constitutes a generic platform for designing bespoken heterostructures between metal layers and technologically relevant weakly-interacting substrates.

I. INTRODUCTION

Vapor-based synthesis of thin noble-metal films and nanostructures on oxides and van der Waals materials is a key step for fabricating heterostructure devices in the areas of nanoelectronics,[1,2] biosensing,[3] catalysis,[4,5] energy saving,[6] and energy conversion.[7–9] The performance of these devices depends crucially on the metal film morphology; in some cases, flat two-dimensional (2D) metal-layers that fully wet the underlying substrate are required, while in other cases the objective is to decorate the substate with arrays of three-dimensional (3D) metal nanostructures with well-defined sizes and shapes.[1,2] Achieving such control over the metal film morphology is challenging, as weak interaction (i.e., bond strength) at the interface forming between most metals and oxides

or van der Waals materials provides a strong driving force for uncontrolled formation of 3D metal island agglomerates on the substrate surface.[1,10]

Film synthesis via vapor condensation is characterized by high supersaturation ratios at the vapor/solid interface yielding a far-from-equilibrium growth process, such that film morphological evolution is primarily governed by the occurrence rates of thermally-activated atomistic mechanisms (e.g., surface diffusion and step-edge crossing).[11–14] Extensive research over the past 30 years has painted a detailed atomic-scale picture of growth in homo- and heteroepitaxial film/substrate systems, including noble metals.[14] This understanding has led to the development of methodologies for navigating between 2D and 3D morphology, which are based on deployment of minority species that float on the film surface (also known as *surfactants*) and modify atomic-scale kinetics at the film-growth front.[15–20]

The atomistic processes that control film morphological evolution in weakly-interacting film/substrate systems are fundamentally different than those in epitaxy. For instance, formation of 3D islands on weakly-interacting surfaces requires upward atomic transport,[10,21,22] while roughness buildup in epitaxy is the result of strain relaxation[11,12] or limited interlayer transport mediated by the step-edge descent barrier.[14] Hence, state-of-the-art surfactant-based strategies are not unconditionally relevant for manipulating film growth on weakly-interacting substrates. Despite the latter, empirical studies have shown that the use transition-metal and semiconducting alloying agents and seed layers,[23–29] as well deployment of gaseous species[9,30–35] can effectively reverse the tendency toward 3D morphology in Ag and Cu layers on oxide substrates. Concurrently, potential incorporation of alloying species in the film, as well as modification of the film/substrate

interface due to the presence of seed layers may affect other physical (e.g., optoelectronic) properties of the noble-metal layer and the overall performance of the corresponding heterostructure device.[24] These shortcomings, if not reversed or mitigated, render such strategies largely inapplicable for synthesizing device-relevant weakly-interacting heterostructures.

Using as foundation pioneering work from past decades,[36–45] we have studied growth in weakly-interacting film/substrate systems and identified key structure-forming processes that govern 3D morphological evolution during island nucleation, growth, and coalescence.[22,53–60] Inspired by these studies and guided by *in situ* and real-time monitoring of film growth by spectroscopy ellipsometry,[61] we have recently developed a versatile concept for growth manipulation using magnetron-sputter deposited Ag on SiO_2 as a model system. This concept entails the use of minority species—both gases (N_2,O_2)[62,63] and less-noble-metal alloying agents(Cu)[64]—which are *deployed selectively* to target specific film-formation stages and either promote 2D metal-layer morphology without compromising its electrically conductivity, or enhance 3D morphology at a given set of process parameters.

In the present article, we expand upon our growth manipulation concept by exploring the viability of a multitude of metallic alloying species, that include Au, Al, Cr, Ti, Mo (the motivation for the alloying agent selection is provided in Section III; data for Cu are taken from Ref. 64 and are presented here for comparison). We show that selective deployment of alloying agents represents a generic platform for efficient and non-invasive growth manipulation that allows to design bespoken noble-metal layers by choosing minority species, based on their ability to meet specific application-relevant

requirements, e.g., optoelectronic properties, chemical affinity to ambient contaminants, and cost.

II. EXPERIMENTAL STRATEGY AND PROCEDURES

A. Film synthesis

Ag and Ag-alloy films (hereinafter denoted as Ag and AgX, respectively, whereby X = Cu, Au, Al, Cr, Ti, Mo) are synthesized in an ultra-high vacuum chamber (base pressure ~10^{-8} Pa). The chamber is equipped with three confocally-arranged magnetron sources that form an angle of 45° with respect to the substrate surface normal (see Fig.1 for a 2D illustration). Substrates are Czochralski-grown n-type Si(100) wafers, covered with a ~490-540 nm thick thermally-grown SiO_2 layer. No intentional substrate heating is used during the depositions. Ag and alloying species X vapors are generated by sputtering two magnetron sources (placed at a distance 7.5 cm from the substrate; Ar sputtering gas pressure is equal to 1.3 Pa) which are equipped with the respective Ag and X elemental targets (target diameter 7.6 cm; target purity better than 99.95%). The magnetrons are supplied with electrical power (time-averaged value ~10 W) in the form of 50 μs long unipolar voltage pulses, with a frequency of 1 kHz. The X-to-Ag atom arrival ratio on the film surface is controlled by varying the voltage of the alloy target magnetron $V_{T,X}$ between 225 and 400 V, while $V_{T,Ag}$ is held constant at 485 V. Moreover, the electrical signal of $V_{T,Ag}$ is used to trigger $V_{T,X}$. In that way, the voltage pulses applied on both magnetrons and, thereby, the arrival of Ag and X vapor at the substrate are synchronous, such that any changes in film morphological evolution cannot be ascribed to random variations of the deposition flux temporal profile.[65,66]

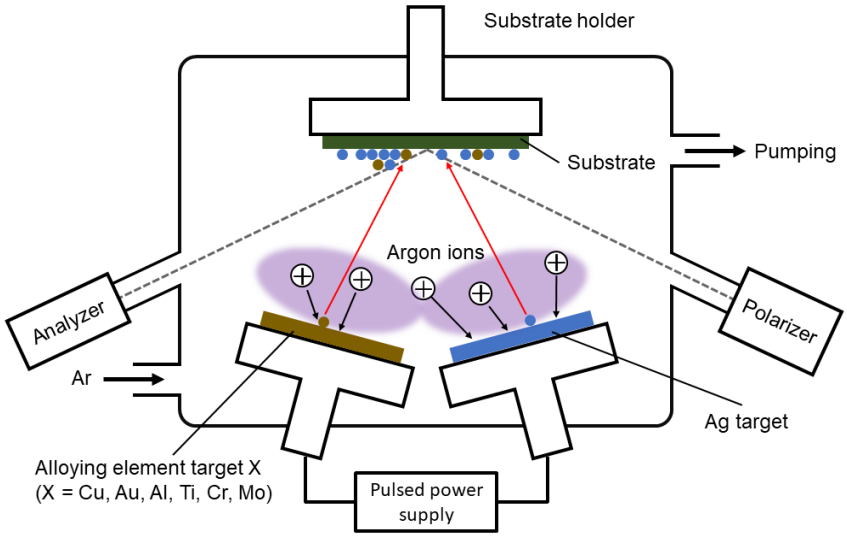

FIG. 1. Schematic illustration of the deposition setup used for film synthesis and *in situ* growth monitoring. More information for the various components of the setup can be found in the text.

As explained in Section I, our growth manipulation strategy is based on selective deployment of minority species to target specific film-formation stages. This concept is implemented by using the following schemes (see Fig.2 for a schematic illustration): (i) alloying species are deposited together with Ag throughout the entire growth process (Scheme 1); (ii) alloying atoms are deployed at the early film-growth stages so that the growth surface is exposed to their presence for a time t_E ranging between 2 to 20 s. Subsequently, the operation of the magnetron source equipped with the alloying element target is terminated, while growth continues and is completed with Ag vapor flux only (Scheme 2); and (iii) deposition commences with Ag vapor flux and, after a delay time t_D ranging from 2 to 20 s, alloying agent vapor is co-deposited with Ag for the remainder of the growth (Scheme 3).

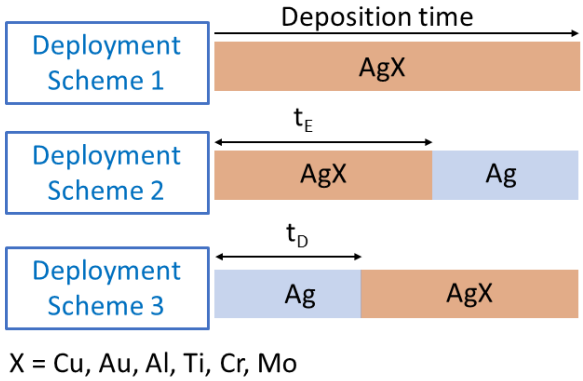

FIG. 2. Schematic illustration of alloying agent X (X = Cu, Au, Al, Ti, Cr, Mo) deployment strategies. Scheme 1: Alloying species are deployed during the entire duration of film growth. Scheme 2: Alloying species are deployed only for an initial time t_E in the range 2 to 20s. Scheme 3: Alloying species are deployed after a delay time t_D ranging from 2 to 20 s.

B. *In situ film growth monitoring*

The development and evaluation of the growth manipulation concept demonstrated in the present paper is largely based on real-time monitoring of film morphological evolution. This is achieved using spectroscopic ellipsometry, a non-destructive optical technique that determines the optical properties of materials by measuring changes in the polarization state of a light beam upon its interaction with the sample under investigation.[67] The methodology used for collecting and analyzing ellipsometric data has been explained in detail in our previous studies,[61–64] hence here we only summarize key aspects.

Ellipsometric spectra are collected every ~2 s in the photon energy range 1.6 to 3.2 eV, at an angle of incidence of 70° from the substrate surface normal, using a rotating analyzer instrument that is mounted to the sputter deposition chamber (see Fig.1). The

acquired time-dependent data are fitted to a three-phase model consisting of vacuum, metal-layer, and substrate.

We analyze data corresponding to: (i) initial film growth stages in which the substrate surface features isolated metal islands; and (ii) percolated metal layers that exhibit electrical conductivity. In the former case, the optical response of the film is described using a Lorentz oscillator,[68] to account for localized surface plasmon resonance effects.[69] Conducting layers are modelled using the Drude free electron theory.[68] From the two models we extract the oscillator resonance frequency $\hbar\omega_0$ (Lorentz) and the room-temperature resistivity ρ (Drude), and by studying their changes as a function of deposition time t we draw conclusions with regards to film morphological evolution (see Section III for details).

Besides $\hbar\omega_0$ and ρ, the ellipsometric analysis also provides the film heigh h_f as a function of t. We plot h_f vs. t curves and use their steady-state slope (i.e., the slope that corresponds to growth of a continuous layer) to extract the film deposition rate F ($F \approx 0.12$ nms^{-1} at all conditions used in this work). Based on the calculated deposition rate, the nominal film thickness Θ (i.e., the amount of deposited material) at any given time during growth is computed as $\Theta = F \times t$. Throughout the manuscript, Θ is expressed in monolayers (ML), whereby 1 ML = 0.235 nm (Ag (111) interplanar spacing, which is the most common out-of-plane orientation for physical vapor deposited face-centered-cubic (fcc) metal films[13]).

C. *Ex situ characterization*

In situ characterization is complemented by *ex situ* imaging of discontinuous film surfaces using a Field Emission Gun Scanning Electron Microscope (SEM), at an operating voltage of 4 kV and a working distance of 3 mm. SEM images are analyzed using the ImageJ software package,[70] to determine the fraction of the substrate covered by the film. Real-space imaging is combined with X-ray diffractometry (XRD) to determine the crystal structure of the deposited metal layers. XRD measurements are performed in Bragg-Brentano geometry using a Goebel mirror for the incident beam, and a copper K_α source (wavelength 0.15418 nm) in line focus. Film chemical composition is determined by energy-dispersive x-ray spectroscopy (EDX) measurements which are carried out in the same apparatus as the one used for SEM analysis. EDX composition for selected samples is cross-checked by x-ray photoelectron spectroscopy (XPS), which also provides information about the film bonding configuration. XPS measurements are carried using an AXIS Ultra spectrometer in a UHV system (base pressure ~10^{-8} Pa), equipped with a monochromated aluminum K_α x-ray beam. Photoelectron spectra are collected as a function of the sample depth using 4 keV Ar^+ ion-beam etching. We note that prior to transferring samples to the *ex situ* characterization equipment, a capping 3 nm-thick amorphous carbon layer is sputter-deposited (in the same chamber as the one used of film growth; see Fig.1) to avoid surface contamination and changes in film morphology upon atmospheric exposure.

III. RESULTS AND DISCUSSION

The first step for exploring the propensity of the various metal alloying agents to affect Ag-layer morphological evolution is to perform experiments in which alloying species are deposited together with Ag throughout the entire growth process (deployment Scheme 1 in Fig.2). Figure 3 plots ρ vs. Θ curves extracted from analysis of *in situ* ellipsometry data, which are collected during such experiments, for Ag layers and AgX films with composition $Ag_{0.96}X_{0.04}$. For all curves, the resistivity ρ exhibits an initial sharp drop after which it reaches a steady-state value ρ^{ss}. We have previously shown that[53,54,57,61]: (i) the nominal thickness at which ρ^{ss} is established (denoted as Θ_{cont}) signifies the formation of continuous layer; and (ii) the magnitude Θ_{cont} can be used as a proxy for assessing the character of growth, i.e., decrease of Θ_{cont} indicates that the film grows flatter and 2D morphology is promoted. The data show that all alloying elements used yield Θ_{cont} values that are smaller than that of pure Ag (Θ_{cont} = 81 ML; black squares), with the maximum decrease achieved for the case of Cu (Θ_{cont} = 47 ML; red circles). Concurrently, all $Ag_{0.96}X_{0.04}$ films exhibit ρ^{ss} values that are larger than that of pure Ag ($\rho^{ss} = 1.07 \times 10^{-7}$ Ωm), e.g., $\rho^{ss} = 3.87 \times 10^{-7}$ Ωm for $AgTi_{0.04}$ (brown diamonds). All Θ_{cont} and ρ^{ss} values from the curves presented in Fig.3 are listed in Table I. We note here that qualitative similar trends with respect to the effect of alloying agents on Θ_{cont} and ρ^{ss} are obtained for AgX films with content of alloying species up to 20 at. % (i.e., $Ag_{0.8}X_{0.2}$ films). Hence, in the remainder of the article we focus on data for $Ag_{0.96}X_{0.04}$ layers.

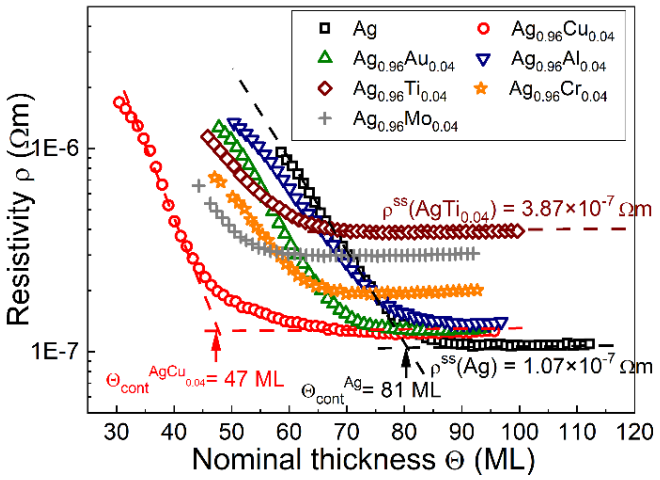

FIG. 3. Resistivity ρ vs nominal thickness Θ for Ag- and $Ag_{0.96}X_{0.04}$-film growth on SiO_2, whereby alloying species X are deployed continuously throughout the entire deposition process. The symbols in the curves correspond to the following alloying agents: Cu (red circles), Au (green triangles), Al (blue inverse triangles), Ti (brown diamonds), Cr (orange stars), Mo (grey crosses). Data corresponding to pure Ag-layer growth are represented by black squares. The position of the continuous film formation thickness Θ_{cont} for the Ag and $AgCu_{0.04}$ curves are marked with vertical arrows, along with the corresponding Θ_{cont} values. The values of the steady-state resistivity ρ^{ss} for Ag and $AgTi_{0.04}$ are provided next to the corresponding curves. Data for $AgCu_{0.04}$ are taken from Ref. 64.

TABLE I. Continuous formation layer (Θ_{cont}) and steady state resistivity (ρ^{ss}) of Ag and $Ag_{0.96}X_{0.04}$ layers extracted from the curves presented in Fig.3. The table also provides bulk resistivity (ρ^{bulk}; Ref. 71) and the homologous temperature T_g/T_m of Ag and alloying species X , as well as the mixing enthalpy for the binary Ag-X system ($\Delta H_{Ag\text{-}X,\,mix}$; Ref. 72).

Layer	Θ_{cont} (ML)	$\rho^{ss} \times 10^{-7}$ (Ωm)	Metal	$\rho^{bulk} \times 10^{-7}$ (Ωm)	T_g/T_m	$\Delta H_{Ag\text{-}X,mix}$ (kJ/mol)

Ag	81	1.07	Ag	0.164	0.24	-
$AgCu_{0.04}$	47	1.23	Cu	0.123	0.22	2
$AgAu_{0.04}$	69	1.28	Au	0.243	0.22	-4.6
$AgAl_{0.04}$	78	1.37	Al	0.279	0.32	-4
$AgTi_{0.04}$	62	3.87	Ti	5.55	0.16	-14
$AgCr_{0.04}$	63	1.97	Cr	6.18	0.14	27
$AgMo_{0.04}$	53	2.99	Mo	6.81	0.1	147

To correlate the trends established in Fig.3 with initial film-formation stages, we study the evolution of the optical properties of discontinuous Ag and $Ag_{0.96}X_{0.04}$ layers (i.e., Lorentz resonance frequency $\hbar\omega_0$) as a function of Θ. Data in the form of $\hbar\omega_0$ vs. Θ curves are plotted in Fig.4, where we observe that for all samples $\hbar\omega_0$ decreases with increasing Θ (i.e., a redshift of the resonance frequency is observed). This behavior is due to in-plane island growth with continued deposition that leads to decrease of the substrate area (surface) coverage and the island-island separation distance.[62,69] Moreover, the $\hbar\omega_0$ values for the $Ag_{0.96}X_{0.04}$ films for a given Θ are smaller than those for pure Ag, while the corresponding $\hbar\omega_0$ vs. Θ curves exhibit a larger declining slope. These findings support the notion that: (i) deployment of alloying agents promote in-plane island growth and thereby 2D morphological evolution, as established from the data in Fig.3 and Table I; and (ii) the film morphology of percolated and continuous layers may be associated with processes occurring during the initial film-formation stages in discontinuous layers for Θ < 30 ML. Exception to the above-explained trends is the $\hbar\omega_0$ vs. Θ curve for $Ag_{0.96}Al_{0.04,}$ which is nearly identical to that of Ag. This is consistent with fact that addition of 4 at.%

of Al leads to only a marginal decrease of the Ag-layer Θ_{cont} from 81 to 78 ML (see Table I).

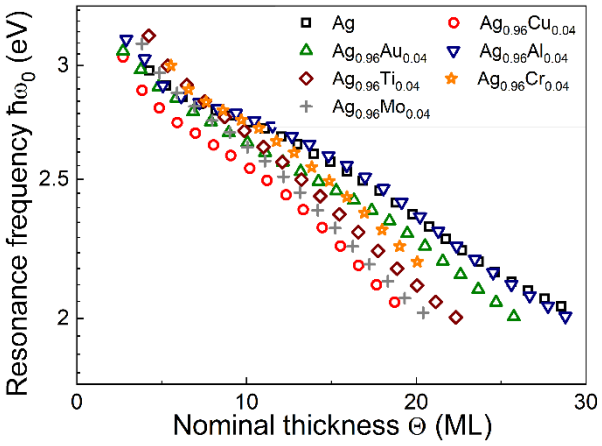

FIG. 4. Lorentz resonance frequency $\hbar\omega_0$ vs. nominal thickness Θ for Ag- and $Ag_{0.96}X_{0.04}$-film growth on SiO_2, whereby alloying species X are deployed continuously throughout the entire deposition process. The symbols in the curves correspond to the following alloying agents: Cu (red circles), Au (green triangles), Al (blue inverse triangles), Ti (brown diamonds), Cr (orange stars), Mo (grey crosses). Data corresponding to pure Ag-layer growth are represented by black squares.

We further study early-stage film morphology by performing SEM analysis of discontinuous Ag and $Ag_{0.96}X_{0.04}$ layers. Top-view SEM micrographs for Ag, $Ag_{0.96}Cu_{0.04}$, and $Ag_{0.96}Ti_{0.04}$ films corresponding the nominal thicknesses Θ = 10, 15, and 25 ML are shown in Fig.5. The data for Ag films (top row) show that initially (Θ = 10 ML) the surface features isolated nearly spherical clusters the size of which increases when increasing Θ to 15 and 25 ML. Moreover, the increase in the cluster size is accompanied by a gradual transition from spherical to more elongated shapes. The latter is consistent with established knowledge of morphological evolution, and it is the result of the dynamic competition between island growth and cluster reshaping rates.[36–45]

Addition of Cu (middle row) and Ti (bottom row) does not modify the overall qualitative film morphological evolution. However, for Θ = 15 and 25 ML the $Ag_{0.96}Cu_{0.04}$, and $Ag_{0.96}Ti_{0.04}$ surfaces exhibit more elongated and interconnected clusters as compared to their pure Ag counterparts. This observation indicates that the deployment of alloying agents hinders material redistribution during coalescence and promotes expansion of islands in the in-plane direction at the expense of out-of-plane growth.

The qualitative analysis of Fig.5 is complemented by calculation of the substrate area coverage q evolution as a function of Θ (q values are provided as insets in the corresponding SEM micrographs). For all films, q increases with increasing Θ, while for each given Θ we see that $q^{Ag_{0.96}Cu_{0.04}}$ and $q^{Ag_{0.96}Ti_{0.04}}$ are larger than q^{Ag}. The latter confirms the conclusion drawn based on the $\hbar\omega_0$ *vs.* Θ curves in Fig.4., i.e., deployment of alloying agents promotes 2D morphological evolution already at the growth stage of coalescence. Hence our findings indicate strongly that alloying agents lead to flatter film formation by hindering island reshaping during coalescence, in agreement with our previous studies[62,63] and recent literature reports.[73] However, we note that other mechanisms, including increase of island density during nucleation[23,24] and/or suppression of upward mass transport during island growth (the latter suggested by McDougall *et al.*[74] for explaining formation of bilayer Dy films on graphene well below room temperature), may also be contributing factors to the observed morphological evolution.

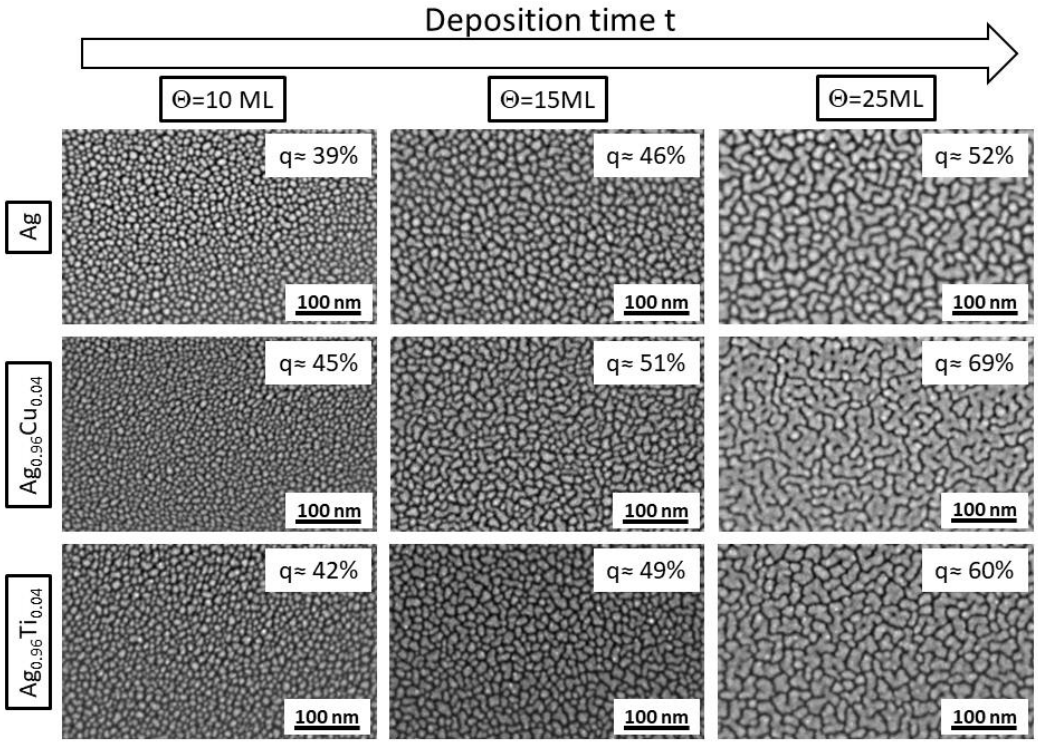

FIG. 5. Top-view SEM micrographs of Ag (top row), $Ag_{0.96}Cu_{0.04}$ (middle row), and $Ag_{0.96}Ti_{0.04}$ (bottom row) layers corresponding to nominal thicknesses Θ = 10, 15, and 25 ML. The substrate area coverage q is provided as inset in each micrograph. Data for Ag and $Ag_{0.96}Cu_{0.04}$ are taken from Ref. 64.

The results presented in Figs. 3 and 4 and listed in Table I (i.e., ρ vs. Θ curves, Θ_{cont} values, and $\hbar\omega_0$ vs. Θ curves) show that the propensity for promoting 2D morphological evolution varies greatly among the various alloying agents. The chosen alloying species exhibit a wide range of bulk melting points T_m,[72] which in the context of thin-film growth is a proxy for atomic mobility.[11–13] Moreover, among the various metals, Cu, Cr, and Mo are immiscible with Ag, while Au, Al, and Ti are miscible.[72] These two aspects, i.e., mobility and miscibility, play a central role for the tendency of alloying atoms to segregate or become incorporated in the Ag grains, and thereby modify local

atomic arrangement and the structure-forming processes at the film growth front. To assess the relevance of such effects, we list on Table I the homologous temperature T_g/T_m for each metal (the growth temperature T_g is taken to be equal to 300 K, as no intentional heating is applied to the substrate during deposition), along with the magnitude of the mixing enthalpy $\Delta H_{Ag\text{-}X,mix}$ for each binary Ag-X combination, whereby positive (negative) $\Delta H_{Ag\text{-}X,mix}$ values denote immiscible (miscible) systems. The general trend observed in Table I is that a decrease in alloying element mobility (i.e., decrease in T_g/T_m) yields a lower Θ_{cont}. Low-mobility alloying atoms may act as pinning sites for adatoms, such that adatom diffusion on facets and material redistribution during coalescence is hindered and 2D growth morphology is promoted.[58] Concurrently, a more complex behavior is observed when considering the effect of miscibility, most notably exemplified by comparing the $AgCu_{0.04}$ and $AgAu_{0.04}$ layers. While Au and Cu exhibit identical T_g/T_m values of 0.22, Cu yields a more pronounced decrease in Θ_{cont} than Au (Θ_{cont} = 69 and 47 ML, for Au and Cu, respectively). XPS analysis (data not presented here) shows that the incorporation of alloying species in the Ag layer does not modify the Ag bonding properties, i.e., no Ag-X bonds and compounds are formed. Hence, the data presented in Table I indicate that immiscible alloying species, which have a larger tendency for segregating at crystal facets and grain boundaries, are potentially more effective in affecting the atomic-scale processes that govern early-stage film morphology. However, further research is required in which additional factors, including crystal structure of the alloying material and alloying species interaction with the substrate and their affinity with impurities need to be considered for establishing a more complete understanding of the effect of minority species on the Ag-layer morphological evolution.

Besides Θ_{cont}, the data in Fig. 3 and in Table I show that the choice of alloying element also affects the value of steady-state resistivity ρ^{ss} of the continuous layer. To understand the correlation between continuous-layer optoelectronic properties and bulk conductivity of the alloying agent material, we also list in Table I the bulk resistivity ρ^{bulk} of the various metals ρ^{bulk} values taken from Ref. 71). The data show a correlation between ρ^{ss} and ρ^{bulk}, e.g., the largest ρ^{ss} is obtained when using as alloying species refractory metals (Ti, Cr, Mo) which intrinsically exhibit relatively large ρ^{bulk} values. This indicates that the electron transport properties of AgX layers may be governed by changes in bulk electron mobility and density caused by the presence of minority species in the film.[75]

Another factor that affects electrical conductivity of ultra-thin metal layers is scattering of charge carriers at interfaces, i.e., film surface and grain boundaries, which typically lead to larger resistivities in relation to the corresponding bulk values (see e.g., comparison between ρ^{ss} and ρ^{bulk} for Ag in Table I).[75] To investigate possible effects of alloying agents on the Ag-layer crystal structure and its correlation with the film conductivity, we performed XRD measurements. XRD patterns of 50 nm thick Ag and $Ag_{0.96}X_{0.04}$ films in the angular range 35 to 45° are plotted in Fig.6, where the position of (111) and (200) reflections for bulk unstrained Ag[76] are marked with vertical lines. There we see that all films exhibit the fcc crystal structure of Ag with strong (111) out-of-plane orientation irrespective of layer composition. We also observe that (111) reflections are broader in $Ag_{0.96}X_{0.04}$ as compared to Ag, i.e., incorporation of alloying species causes grain refinement, the latter being another mechanism that can explain the increase of ρ^{ss} in $Ag_{0.96}X_{0.04}$ layers.

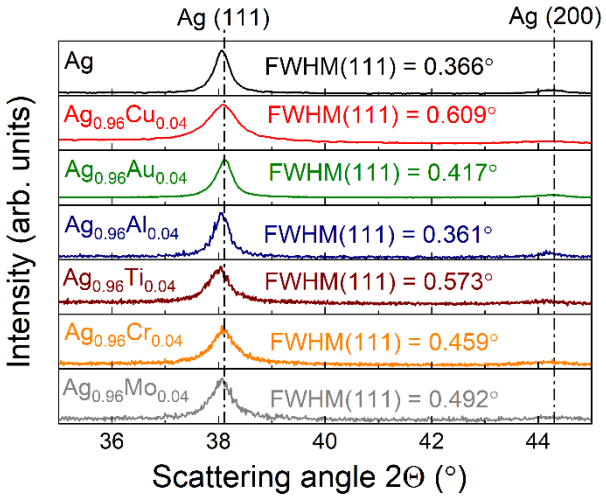

FIG. 6. Bragg-Brentano XRD patterns of Ag and $Ag_{0.96}X_{0.04}$ films. The angular position of the Ag (111) and Ag (200) diffraction peaks is marked by vertical lines. The full width at half maximum (FWHM) of the corresponding Ag (111) is provided on each panel.

The results presented so far show that changes in film morphological evolution upon alloying agent deposition are correlated with processes occurring during the initial film growth stages. Hence, in the following we explore the viability of growth manipulation via selective deployment of minority species, in accordance with our previous studies.[62–64] Films were grown by either introducing minority species at the beginning of deposition for a time t_E (Deployment Scheme 2 in Fig. 2), or after having deposited Ag vapor for a time t_D (Deployment Scheme 3 in Fig. 2). Representative data in the form of ρ vs. Θ curves (recorded during Ag and AgX film growth) for $t_E = 20$ *s* ($Ag_{0.96}X_{0.04}$ (20s) + Ag) and t_D = 20 s (Ag (20s) + $Ag_{0.96}X_{0.04}$) are displayed in Figs.7(a) through (c). The data for $t_E = 20$ *s* show that the early deployment of all alloying species X leads to a decrease of the Θ_{cont} relative to pure Ag, i.e., 2D morphology is promoted (Fig.7(a)). Moreover, non-invasive growth manipulation, i.e., decrease of Θ_{cont} without increase of continuous-layer resistivity ρ^{ss}, is achieved for Cu, Au, and Al, which

according to Table I and Fig.3 are the minority species that have the least effect of the Ag conductivity. Whilst a slight decrease in ρ^{ss} is observed for Ti, Cr, and Mo (e.g., 1.31×10^{-7} Ωm for the case of Ti vs. 1.07×10^{-7} Ωm for pure Ag; see Fig.7(b)). The data corresponding to deployment after the first 20 s of deposition (Fig.7(c)) show that all alloying species lead to larger ρ^{ss} values relative to the reference Ag film. However, differences with regards to the character of growth are observed: Cu, Au, Al, and Cr promote 2D morphology, while Ti and Mo favor 3D growth. The former group of metals exhibits similar behavior as that observed when O_2 is used for growth manipuation,[63] while the effect of the latter group of metals is reminiscent to that of N_2.[62] The origin of this behavior is currently unknown but indicates that metals affect in a complex manner the post-coalescence processes of hole-filling and crystal growth, and it calls for dedicated experimental and theoretical studies to understand these phenomena on a fundamental atomistic level.

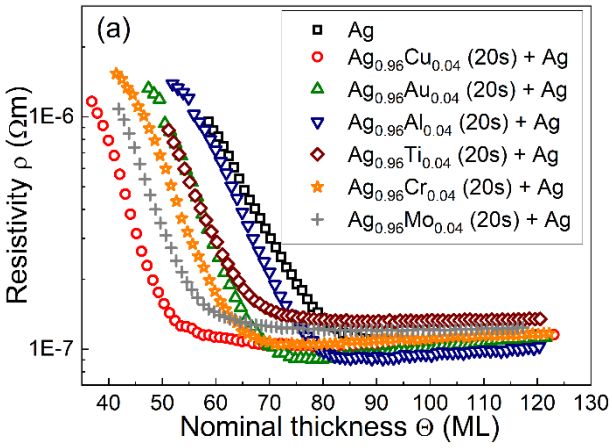

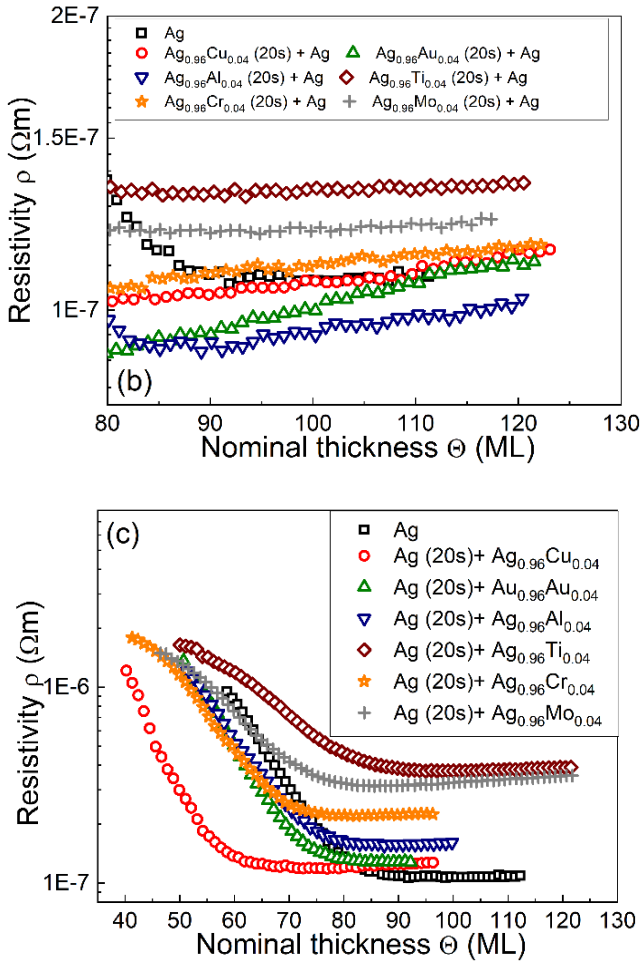

FIG. 7. Resistivity ρ vs nominal thickness Θ for Ag and AgX layer growth on SiO_2, whereby alloying agents X are deployed: (a), (b) during the initial $t_E = 20\ s$ of deposition ($Ag_{0.96}X_{0.04}$ (20s) + Ag), with panel (b) presenting a zoom into the area of steady-state resistivity ρ^{ss} to better discern the differences among the various curves; and (c) after a time $t_D = 20\ s$ from the beginning of the deposition (Ag (20s) + $Ag_{0.96}X_{0.04}$). The symbols in the curves correspond to the following alloying species: Cu (red circles), Au (green triangles), Al (blue inverse triangles), Ti (brown diamonds), Cr (orange stars), Mo (grey crosses). Data corresponding to growth of pure Ag layers are represented by black squares. Data for the case of Ag-layer growth modified by selective deployment of Cu are taken from Ref. 64.

IV. SUMMARY AND CONCLUSIONS

Growth of thin noble-metal films on weakly-interacting substrates is typically characterized by an intrinsic tendency toward uncontrolled formation of 3D metal island agglomerates, which is an obstacle for fabricating high-performance heterostructure devices. Here we demonstrate a versatile concept for manipulating growth morphology between 3D and 2D using Ag/SiO_2 as a weakly-interacting film/substrate model system. This concept entails deployment of metallic (Cu, Au, Al, Ti, Cr, Mo) alloying species at the film growth front with the purpose of modifying fundamental structure-forming processes.

Data from *in situ* and real-time monitoring of film growth using spectroscopic ellipsometry reveal that release of alloying agents from the onset of Ag-layer deposition until its completion promotes 2D morphology, as compared to pure Ag growth. However, this comes at the expense of the AgX layer conductivity which is lower than that obtained for alloying-agent-free growth. The ability of alloying species to favor 2D growth phenomenologically depends on their melting point, whereby metallic species X with higher melting temperatures yield flatter Ag layers. In addition, alloying atoms that are immiscible with Ag are more effective at promoting 2D morphology. Moreover, *ex situ* analyses of the surface of discontinuous layers show that AgX film growth is characterized by a slower (relative to pure Ag films) reshaping of clusters during island coalescence, which can explain the tendency towards 2D morphological evolution.

Inspired by these findings and our previous studies,[62–64] we present a concept in which alloying agents are deployed with high temporal precision, to selectively target

film-formation stages before and after island coalescence completion. We show that all alloying species, when present only during the initial pre-coalescence growth stages, favor 2D growth morphology with no (X = Cu, Al, Au) or small (X = Ti, Cr, Mo) effect on the Ag-layer conductivity, i.e., non-invasive growth manipulation is achieved. However, when alloying atoms are deployed after island coalescence completion a more complex behavior is observed: Cu, Au, Al, and Cr favor 2D growth, while Ti, and Mo cause a transition to a rougher film with considerably lower conductivity.

We have previously demonstrated the use of N_2[62] and O_2[63] gaseous species for manipulating growth of Ag on SiO_2. This approach, although effective on a conceptual level, may not be relevant in practice, e.g., accurate control of the deployment pattern of gases in large-scale deposition setups might be challenging. This is because slow pumping speeds may render transient times between gas compositions comparable with the duration of the film deposition, while flow gradients may lead to variations in the gas partial pressures in the vicinity of the target and the substrate. These challenges may be mitigated by using metallic alloying agents, as demonstrated in the present study. In a broader context, the overall results presented herein are the first step towards developing a generic platform for synthesizing weakly-interacting heterostructures with bespoken morphology and thereby physical properties. This platform will be founded upon appropriate selection of alloying agents and deployment schemes to either promote 2D morphology in a non-invasive fashion or favor 3D growth without changing other processing conditions (e.g., temperature). Moreover, navigating across a wide range of possible alloying materials allows optimizing heterostructure design by taking into consideration technological requirements that include material cost, availability,

environmental stability, and affinity to impurities. This is of paramount importance in a number of devices based on weakly-interacting film/substrate systems, such as energy-saving windows, catalysts, and nanoelectronic components.

ACKNOWLEDGMENTS

KS acknowledges financial support from the Swedish research council (contracts VR-2015-04630 and VR-2021-04113). AJ and KS acknowledge financial support from the Åforsk foundation (contract ÅF 19-137). NP and KS acknowledge financial support from the Olle Engkvist foundation (contract SOEB 190-31) and the Wenner-Gren foundations (contracts UPD2018-0071 and UPD2019-0007). AJ and GA acknowledge financial support of the French Government program “Investissements d’Avenir” (LABEX INTERACTIFS, reference ANR-11-LABX-0017-01).

DATA AVAILABILITY

Raw data corresponding to the results presented in the manuscript are available by contacting the corresponding author.

AUTHOR DECLARATIONS

Conflict of Interest

The authors have no conflicts to disclose.

Author contributions

AJ and NP performed film growth and characterization experiments and analyzed experimental data. KS and GA planned and supervised the research. KS wrote the article. All authors contributed to the interpretation of the experimental results and critically reviewed and provided input to the manuscript.

REFERENCES

[1] X. Liu, Y. Han, J.W. Evans, A.K. Engstfeld, R.J. Behm, M.C. Tringides, M. Hupalo, H.-Q. Lin, L. Huang, K.-M. Ho, D. Appy, P.A. Thiel, and C.-Z. Wang, Prog. Surf. Sci. **90**, 397 (2015).

[2] C. Gong, C. Huang, J. Miller, L. Cheng, Y. Hao, D. Cobden, J. Kim, R.S. Ruoff, R.M. Wallace, K. Cho, X. Xu, and Y.J. Chabal, ACS Nano **7**, 11350 (2013).

[3] Y. Xu, C.-Y. Hsieh, L. Wu, and L.K. Ang, J. Phys. D. Appl. Phys. **52**, 065101 (2019).

[4] D. Deng, K.S. Novoselov, Q. Fu, N. Zheng, Z. Tian, and X. Bao, Nat. Nanotechnol. **11**, 218 (2016).

[5] T.A. Shifa, F. Wang, Y. Liu, and J. He, Adv. Mater. **31**, 1804828 (2019).

[6] K. Kato, H. Omoto, T. Tomioka, and A. Takamatsu, Sol. Energy Mater. Sol. Cells **95**, 2352 (2011).

[7] G. Zhao, S.M. Kim, S.-G. Lee, T.-S. Bae, C. Mun, S. Lee, H. Yu, G.-H. Lee, H.-S. Lee, M. Song, and J. Yun, Adv. Funct. Mater. **26**, 4180 (2016).

[8] G. Zhao, W. Shen, E. Jeong, S.-G. Lee, H.-S. Chung, T.-S. Bae, J.-S. Bae, G.-H. Lee, J. Tang, and J. Yun, ACS Appl. Mater. Interfaces **10**, 40901 (2018).

[9] W. Wang, M. Song, T.-S. Bae, Y.H. Park, Y.-C. Kang, S.-G. Lee, S.-Y. Kim, D.H. Kim, S. Lee, G. Min, G.-H. Lee, J.-W. Kang, and J. Yun, Adv. Funct. Mater. **24**, 1551

(2014).

[10] C.T. Campbell, J. Chem. Soc. Faraday Trans. **92**, 1435 (1996).

[11] M. Ohring, *The Materials Science of Thin Films* (San Diego, 1992).

[12] P.M. Martin, *Handbook of Deposition Technologies for Films and Coatings* (William Andrew, Amsterdam, 2010).

[13] I. Petrov, P.B. Barna, L. Hultman, and J.E. Greene, J. Vac. Sci. Technol. A Vacuum, Surfaces, Film. **21**, S117 (2003).

[14] T. Michely and J. Krug, *Islands, Mounds and Atoms*, 1st ed. (Springer-Verlag Berlin Heidelberg, Berlin, Heidelberg, 2004).

[15] H.A. van der Vegt, H.M. van Pinxteren, M. Lohmeier, E. Vlieg, and J.M.C. Thornton, Phys. Rev. Lett. **68**, 3335 (1992).

[16] H.A. van der Vegt, M. Breeman, S. Ferrer, V.H. Etgens, X. Torrelles, P. Fajardo, and E. Vlieg, Phys. Rev. B **51**, 14806 (1995).

[17] J. Vrijmoeth, H.A. van der Vegt, J.A. Meyer, E. Vlieg, and R.J. Behm, Phys. Rev. Lett. **72**, 3843 (1994).

[18] B. Poelsema, R. Kunkel, N. Nagel, A.F. Becker, G. Rosenfeld, L.K. Verheij, and G. Comsa, Appl. Phys. A Solids Surfaces **53**, 369 (1991).

[19] B. Voigtländer and A. Zinner, Surf. Sci. Lett. **292**, L775 (1993).

[20] M. Horn-von Hoegen, J. Falta, M. Copel, and R.M. Tromp, Appl. Phys. Lett. **66**, 487 (1995).

[21] K. Sarakinos, Thin Solid Films **688**, 137312 (2019).

[22] B. Lü, G.A. Almyras, V. Gervilla, J.E. Greene, and K. Sarakinos, Phys. Rev. Mater. **2**, 063401 (2018).

[23] A. Anders, E. Byon, D.-H. Kim, K. Fukuda, and S.H.N. Lim, Solid State Commun. **140**, 225 (2006).

[24] D. Gu, C. Zhang, Y.-K. Wu, and L.J. Guo, ACS Nano **8**, 10343 (2014).

[25] A. Ciesielski, L. Skowronski, E. Górecka, J. Kierdaszuk, and T. Szoplik, Beilstein J. Nanotechnol. **9**, 66 (2018).

[26] H. Liu, B. Wang, E.S.P. Leong, P. Yang, Y. Zong, G. Si, J. Teng, and S.A. Maier, ACS Nano **4**, 3139 (2010).

[27] C. Furgeaud, L. Simonot, A. Michel, C. Mastail, and G. Abadias, Acta Mater. **159**, 286 (2018).

[28] J. Bulír, M. Novotný, A. Lynnykova, J. Lančok, M. Bodnár, and M. Škereň, in *Proc. SPIE*, edited by R.J. Martin-Palma, Y.-J. Jen, and A. Lakhtakia (2010), p. 77660Q.

[29] M. Messaykeh, S. Chenot, P. David, G. Cabailh, J. Jupille, A. Koltsov, and R. Lazzari, Cryst. Growth Des. **21**, 3528 (2021).

[30] G. Zhao, W. Wang, T.-S. Bae, S.-G. Lee, C. Mun, S. Lee, H. Yu, G.-H. Lee, M. Song, and J. Yun, Nat. Commun. **6**, 8830 (2015).

[31] J.M. Riveiro, P.S. Normile, J.P. Andrés, J.A. González, J.A. De Toro, T. Muñoz, and P. Muñiz, Appl. Phys. Lett. **89**, 201902 (2006).

[32] A.J. Birnbaum, C. V. Thompson, J.C. Steuben, A.P. Iliopoulos, and J.G. Michopoulos, Appl. Phys. Lett. **111**, 163107 (2017).

[33] J. Bulíř, M. Novotný, J. Lančok, L. Fekete, J. Drahokoupil, and J. Musil, Surf. Coatings Technol. **228**, S86 (2013).

[34] R.H.H. Ko, A. Khalatpour, J.K.D. Clark, and N.P. Kherani, APL Mater. **6**, 121112 (2018).

[35] J. Yun, H.-S. Chung, S.-G. Lee, J.-S. Bae, T.E. Hong, K. Takahashi, S.M. Yu, J. Park, Q. Guo, G.-H. Lee, S.Z. Han, Y. Ikoma, and E.-A. Choi, Nanoscale **12**, 1749 (2020).

[36] P. Meakin, Reports Prog. Phys. **55**, 157 (1992).

[37] G. Jeffers, M.A. Dubson, and P.M. Duxbury, J. Appl. Phys. **75**, 5016 (1994).

[38] J. Carrey and J.-L. Maurice, Phys. Rev. B **63**, 245408 (2001).

[39] X. Yu, P.M. Duxbury, G. Jeffers, and M.A. Dubson, Phys. Rev. B **44**, 13163 (1991).

[40] M.C. Bartelt and J.W. Evans, Surf. Sci. **298**, 421 (1993).

[41] J.G. Amar, F. Family, and P.-M. Lam, Phys. Rev. B **50**, 8781 (1994).

[42] F.A. Nichols and W.W. Mullins, J. Appl. Phys. **36**, 1826 (1965).

[43] F.A. Nichols, J. Appl. Phys. **37**, 2805 (1966).

[44] N. Combe, P. Jensen, and A. Pimpinelli, Phys. Rev. Lett. **85**, 110 (2000).

[45] A.D. Brailsford and N.A. Gjostein, J. Appl. Phys. **46**, 2390 (1975).

[46] F. Family and P. Meakin, Phys. Rev. A **40**, 3836 (1989).

[47] L.Ç. Arslan, C. Sanborn, E. Anzenberg, and K.F. Ludwig, Phys. Rev. Lett. **109**, 106102 (2012).

[48] W.W. Mullins and G.S. Rohrer, J. Am. Ceram. Soc. **83**, 214 (2000).

[49] S. Grachev, M. de Grazia, E. Barthel, E. Søndergård, and R. Lazzari, J. Phys. D. Appl. Phys. **46**, 375305 (2013).

[50] D.N. McCarthy and S.A. Brown, Phys. Rev. B **80**, 064107 (2009).

[51] J. Carrey and J.-L. Maurice, Phys. Rev. B **65**, 205401 (2002).

[52] J.M. Warrender and M.J. Aziz, Phys. Rev. B **76**, 045414 (2007).

[53] B. Lü, V. Elofsson, E.P. Münger, and K. Sarakinos, Appl. Phys. Lett. **105**, 163107 (2014).

[54] V. Elofsson, B. Lü, D. Magnfält, E.P. Münger, and K. Sarakinos, J. Appl. Phys. **116**, 044302 (2014).

[55] B. Lü, E.P. Münger, and K. Sarakinos, J. Appl. Phys. **117**, 134304 (2015).

[56] B. Lü, L. Souqui, V. Elofsson, and K. Sarakinos, Appl. Phys. Lett. **111**, 084101 (2017).

[57] A. Jamnig, D.G. Sangiovanni, G. Abadias, and K. Sarakinos, Sci. Rep. **9**, 6640 (2019).

[58] V. Gervilla, G.A. Almyras, B. Lü, and K. Sarakinos, Sci. Rep. **10**, 2031 (2020).

[59] V. Gervilla, M. Zarshenas, D.G. Sangiovanni, and K. Sarakinos, J. Phys. Chem. Lett. **11**, 8930 (2020).

[60] M. Zarshenas, V. Gervilla, D.G. Sangiovanni, and K. Sarakinos, Phys. Chem. Chem. Phys. **23**, 13087 (2021).

[61] J. Colin, A. Jamnig, C. Furgeaud, A. Michel, N. Pliatsikas, K. Sarakinos, and G. Abadias, Nanomaterials **10**, 2225 (2020).

[62] A. Jamnig, N. Pliatsikas, M. Konpan, J. Lu, T. Kehagias, A.N. Kotanidis, N. Kalfagiannis, D. V. Bellas, E. Lidorikis, J. Kovac, G. Abadias, I. Petrov, J.E. Greene, and K. Sarakinos, ACS Appl. Nano Mater. **3**, 4728 (2020).

[63] N. Pliatsikas, A. Jamnig, M. Konpan, A. Delimitis, G. Abadias, and K. Sarakinos, J. Vac. Sci. Technol. A **38**, 043406 (2020).

[64] A. Jamnig, N. Pliatsikas, G. Abadias, and K. Sarakinos, Appl. Surf. Sci. **538**, 148056 (2021).

[65] V. Elofsson, G.A. Almyras, B. Lü, R.D. Boyd, and K. Sarakinos, Acta Mater. **110**, 114 (2016).

[66] V. Elofsson, G.A. Almyras, B. Lü, M. Garbrecht, R.D. Boyd, and K. Sarakinos, J. Appl. Phys. **123**, 165301 (2018).

[67] R.M.A. Azzam and N.M. Bashara, *Ellipsometry and Polarized Light*, 3rd, reprint ed. (North-Holland Personal Library, 1987).

[68] F. Wooten, *Optical Properties of Solids*, 1st ed. (Academic Press, New York, 1972).

[69] T.W.H. Oates and A. Mücklich, Nanotechnology **16**, 2606 (2005).

[70] C.A. Schneider, W.S. Rasband, and K.W. Eliceiri, Nat. Methods **9**, 671 (2012).

[71] M.A. Ordal, R.J. Bell, R.W. Alexander, L.L. Long, and M.R. Querry, Appl. Opt. **24**, 4493 (1985).

[72] Y.-R. Luo, *Comprehensive Handbook of Chemical Bond Energies*, 1st ed. (CRC Press, Boca Raton, 2007).

[73] G. Zhao, E. Jeong, E.-A. Choi, S.M. Yu, J.-S. Bae, S.-G. Lee, S.Z. Han, G.-H. Lee, and J. Yun, Appl. Surf. Sci. **510**, 145515 (2020).

[74] D. McDougall, H. Hattab, M.T. Hershberger, M. Hupalo, M. Horn von Hoegen, P.A. Thiel, and M.C. Tringides, Carbon N. Y. **108**, 283 (2016).

[75] D. Gall, J. Appl. Phys. **127**, 050901 (2020).

[76] ICDD powder diffraction file no. 00-004-0787; silver.